Applied Mathematical Modelling 150 (2026) 116381

Contents lists available at ScienceDirect

Applied Mathematical Modelling

journal homepage: www.elsevier.com/locate/apm

Semi-analytical modeling of receive transfer function and thermal noise of integrated photonic ultrasound transducers

Sabiju Valiya Valappil [a,*], Peter Harmsma [b], Maurits van der Heiden [c], Martin Verweij [a], Paul van Neer [c]

[a] Faculty of Applied Sciences, Delft University of Technology, Lorentzweg 1, Delft, 2628 CJ, Netherlands
[b] Nederlandse Organisatie voor Toegepast Natuurwetenschappelijk Onderzoek (TNO), Stieltjesweg 1, Delft, 2628CK, Netherlands
[c] Nederlandse Organisatie voor Toegepast Natuurwetenschappelijk Onderzoek (TNO), Oude Waalsdorperweg 63, Den Haag, 2509JG, Netherlands

ABSTRACT

Ultrasound transducers (UTs) are extensively used in several applications across a multitude of disciplines. A new type of UTs namely integrated photonic ultrasound transducers (IPUTs) possess superior performance due to the presence of optical interrogation systems, avoiding electric crosstalk and thermal electronic noise of the sensor. However, a major component of the IPUT's noise floor is its thermal acoustic noise. Several studies have been proposed to characterize IPUTs' behavior; nevertheless, these are either incomplete (model only the thermal noise) or targeted to characterize specific responses such as static behavior, in which the modeled receive transfer function (RTF) is about two orders lower than the experiments. In this study, we develop semi-analytical models based on time-domain finite element analysis and analytical expressions to characterize the RTF and thermal noise-induced noise equivalent pressure of IPUTs. We validate the models by comparing them with the literature, where we obtain a close match between them.

1. Introduction

Ultrasound sensors are extensively used in various applications, such as medical diagnostics [1], non-destructive evaluation [2], flow measurement [3], distance measurement [4], and food processing [5], among others. Since these sensors do not apply ionizing radiation, are often real-time, and are relatively inexpensive, ultrasonic imaging is used as a common medical imaging modality. The global market size for diagnostic medical ultrasound was US$6.7 billion in 2020 and is expected to grow to US$9.3 billion in 2027 [6,7]. Ultrasound sources used in medical imaging have limited transmitted signal strength due to the safety limit. Additionally, the attenuation rate inside the human tissue is high, which drastically decreases the signal strength during deep-tissue imaging. Thus, the receivers need to possess a high signal-to-noise ratio (SNR), for which a significant transfer function (the output response due to the incoming pressure) and low noise floor are required.

Conventional ultrasound transducers are based on piezoelectric systems that convert acoustic pulses to electrical signals and vice versa [8]. Additionally, micro-electronic mechanical systems (MEMS)-based transducers are also being used for medical imaging. These transducers are divided into capacitive micromachined ultrasonic transducers (CMUTs) [9] and piezoelectric micromachined ultrasonic transducers (PMUTs) [10] depending on the physical signal conversion principle. CMUTs rely on capacitive changes while PMUTs use thin-film piezoelectric layers to convert the membrane deformation to electrical pulses. The noise equivalent pressure (NEP)—the pressure value for which the SNR is unity—for the aforementioned devices operating around 1 MHz with 80 % −6 dB

* Corresponding author.
E-mail addresses: S.ValiyaValappil@tudelft.nl (S.V. Valappil), peter.harmsma@tno.nl (P. Harmsma), maurits.vanderheiden@tno.nl (M. van der Heiden), M.D.Verweij@tudelft.nl (M. Verweij), paul.vanneer@tno.nl (P. van Neer).

https://doi.org/10.1016/j.apm.2025.116381
Received 9 January 2025; Received in revised form 30 July 2025; Accepted 19 August 2025

Available online 25 August 2025

bandwidth (BW) is comparable to the standard piezoelectric-based ultrasound transducers, which is around 0.5 Pa [9,11,12]. Additionally, their transmit transfer functions are also in the same order, while their noise floor is limited by the thermal electric noise, which is much higher than their thermal acoustic noise (due to their limited size). A novel type of ultrasound transducers – integrated photonic ultrasound transducers (IPUTs) may sidestep the traditional transducer design trade-offs and limitations as they are based on different physical principles.

IPUTs consist of a mechanical resonator combined with an optical integrated photonic circuit. The transfer function of the optical circuit is modified by the incoming pressure wave, which excites the mechanical resonator. This change in the optical transfer function can be measured using optical read-out concepts, for example using a laser [13]. Depending on the IPUT design and the intended read-out chain, they are generally classified as interferometer-based, such as a Mach-Zehnder interferometer (MZI) [14], and whispering gallery mode-based as in the case of a ring resonator (RR) [15]. MZIs comprise a sensing optical waveguide (attached to the mechanical resonator) and a reference optical waveguide. An optical probe signal emitted by a laser is distributed over the sensing- and reference waveguides. The signals from both arms interfere in a combiner, the output signals of which depend on the phase difference between the two paths. When the incoming acoustic pressure impinges on the IPUT, the sample waveguide deforms more than the reference waveguide because the former is on top of the mechanical resonator at or close to resonance. The deformation induces a length change and an effective refractive index change, leading to a phase shift between the reference and sensing signals. This phase shift is detected as an intensity variation at the interferometer outputs, which can be used to measure the incoming pressure. On the other hand, RR-based IPUTs feature a ring-shaped optical waveguide directly connected to the mechanical resonator. This ring-shaped waveguide forms a high-Q factor optical resonator with a series of resonance wavelengths having equidistant spacing in terms of optical frequency. Again, an acoustical pressure wave deforms the IPUT mechanical resonator, affecting both the length and effective refractive index of the optical resonator. This results in a shift of the optical resonance wavelengths. By applying a laser on the steep flank of one such resonance, the aforementioned wavelength shift can be measured as an optical intensity change at the laser wavelength. The relation between the IPUT's measured quantity (e.g., optical phase shift) and the incident field (acoustic pressure) is described as its receive transfer function (RTF).

Several studies have been conducted to model the transfer function of IPUTs and similar optomechanical pressure sensors [16–19]. It is noteworthy that low-frequency opto-mechanical sensors are classified as pressure sensors. On the other hand, optomechanical sensors capable of detecting pressure pulses on or above ultrasound frequencies (i.e. above 20 kHz) are deemed as IPUTs. Jansen et al. proposed an MZI-based optomechanical pressure sensor with high measurement accuracy, where a theoretical model based on the static response of the membrane is used [16]. Since the static model will not be able to predict the dynamic behavior of the IPUTs, Zunic et al. [18] used an acousto-mechanical finite element model with analytical equations to design an IPUT consisting of a silicon nitride MZI placed on a silicon dioxide (SiO_2) membrane for photoacoustic imaging. Rochus et al. modeled the optomechanical pressure sensors with the presence of residual stress using the finite element method (FEM) [17]. They also proposed an analytical procedure to design micro-opto-mechanical pressure sensors incorporating mechanical nonlinearities [19]. They further extended the MZI-based optomechanical devices to use as accelerometers where the modeling was carried out using FEM and analytical expressions [20]. Gao et al. developed equivalent circuit models for characterizing the behavior of optomechanical microphones that are also based on MZIs [21]. By following a similar modeling approach (FEM and analytical methods), Westerveld et al. studied the dynamic behavior of RR-based optomechanical devices with buckled acoustic membranes [22]. FEM and analytical modeling were further used to characterize other similar devices such as IPUTs with slotted RRs [23,24] and Fabry-Perot resonators [25,26]. However, all aforementioned analytical models either assume a static response of the membrane/plate or are based on the modal behavior of the membrane (considering the first mode). Additionally, all the FEM models listed here consider a harmonic response of the IPUT while also assuming that the membrane is the source, which in principle is not correct. In other words, instead of acoustic pulses arriving from the fluid medium to the IPUT (then radiating back to the fluid), the models assume that the membrane oscillates in the presence of fluid and emits acoustic signals to the fluid medium. Thus, to accurately characterize the IPUT's response, the model should capture a more realistic behavior.

To maximize the IPUT's sensitivity whilst maintaining a frequency bandwidth sufficient for medical imaging, we need to optimize its RTF. Next to this, it is desirable for a medical ultrasound system to have a low NEP. Hence it is important to understand, model, and predict the various noise contributions in an IPUT-based system. The main noise sources in an IPUT include the thermo-mechanical (otherwise called thermal) noise [27] and optical shot noise [28]. The noise generated during the interrogation includes back action noise [29], detector noise [30], laser wavelength jitter noise [31], and the laser relative intensity noise [32]. Additionally, depending on the environment of operation, the surrounding medium (e.g., air or water) can also induce thermal noise due to the Brownian motion of the molecules in the liquid or gas impinging the membrane [33]. The influence of the thermal noise on the sensitivity has been investigated extensively for various types of optomechanical devices because in strain, phase, and ultrasound measurement applications the thermal noise dominates the rest of the noise contributions [34–36]. On the contrary, in the case of optomechanical accelerometers, the optical shot noise dominates the other noises [37,38]. This is because these accelerometers operate at very high mechanical and optical Q-factors resulting in a reduced thermal noise. To accurately evaluate the contributions of these noises in the output signal of the IPUT, they need to be precisely characterized. Additionally, the thermal noise is intrinsic to the IPUT, i.e., it is related to the RTF. Thus, to predict the thermal noise correctly, we need to obtain accurate values for the IPUT's RTF as well. Moreover, to understand the influence of various parameter changes on different noise contributions and the RTF, we need to relate them to a parametric space. To that end, a detailed parametric model is needed. To the best of our knowledge, no accurate models exist that can characterize the actual wave propagation behavior of the IPUTs incorporating the acoustic radiation in the fluid medium. In addition, there are no models available that relate relevant IPUT parameters with the RTF, different noise types, and their interrelations.

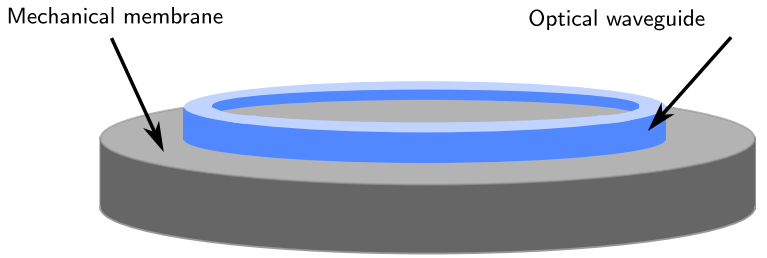

Fig. 1. Schematic representation of an IPUT constituting an optical waveguide (blue ring) and a mechanical membrane (gray disc).

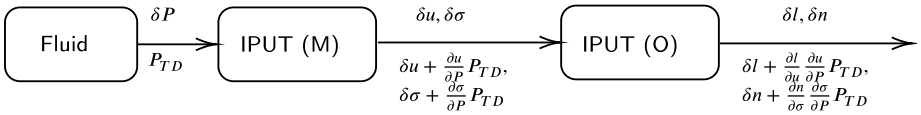

Fig. 2. Transfer function and noise contribution representation in IPUT. M and O, respectively, describe the mechanical and optical components of the IPUT. δP, δu, $\delta\sigma$, δl, and δn, respectively, represent the changes in pressure, membrane displacement (axial), stresses in the membrane, waveguide's length change, and its refractive index change. P_{TD} is the pressure due to the thermal displacement noise at the membrane.

In this work, we present novel semi-analytical models to predict the RTF and noise contribution from the thermal noise of an IPUT in contact with a fluid (water) domain. The model is validated by comparing it to measurement results reported in the literature.

2. Definition and operation of an IPUT sensor

The majority of IPUTs integrate an RR or an MZI on their mechanical resonator. Often the mechanical resonator is a membrane. The modeling approach we employ here is generic to both cases; however, we focus on an RR-based IPUT design for clarity. An RR comprises an optical waveguide looped back to itself. Light from a straight waveguide is coupled to the RR when kept close due to the evanescent field effect. Therefore, an optical resonance with a high Q factor (10^4 to 10^6) occurs when the resonator's optical path length is precisely a whole number of the wavelength. An incoming ultrasound pulse excites the membrane at (or close by) its mechanical resonance. The shift in the wavelength of the optical resonance as a function of the membrane deformation is then monitored. An optical detector placed at the output reads the optical intensity variation and provides the electrical measurements.

In this study, we define the IPUT, as shown in Fig. 1, which is composed of a mechanical resonator (membrane/disc) with an optical waveguide on top. We focus on modeling the deformation of the membrane and the induced changes in the transfer function of the optical waveguide located on top of the membrane. The optical transfer function is affected by the induced changes in length, shape, and refractive index of the waveguide [39]. As our IPUT only includes the membrane and optical waveguide, the noise contributions from the interrogation system, detectors, and other electronic components cannot be evaluated with this IPUT model. Additionally, the optical losses at the couplings from the optical fiber to the IPUT and the effects of the substrate-membrane boundary that can act as an elastic boundary are also neglected here for convenience. The operation of the IPUT is further elaborated next.

The relation between the incoming pressure and the optical intensity—the only optical quantity we can measure using a detector—can be described via the flow diagram shown in Fig. 2. Here, the IPUT is separated into purely mechanical (IPUT (M)) and purely optical (IPUT (O)) components, and their interaction is represented using their independent parameters. The incoming ultrasound pulse from the fluid exerts a pressure load (P) on the IPUT (M) that dynamically deforms the membrane resulting in the displacement of the membrane ($\boldsymbol{u}$) and the development of stresses ($\boldsymbol{\sigma}$) and strains ($\boldsymbol{\epsilon}$). The membrane's displacement further changes the total length of the attached waveguide (δl in IPUT (O)), thus shifting the wavelength corresponding to the waveguide's optical resonant peak. The deformation also alters the cross-sectional area and shape of the waveguide, which influences the effective refractive index of the waveguide (δn). Additionally, the induced stress changes n (effective refractive index) via the photoelastic effect [40], which further modifies the optical path length. This optical resonance shift is converted to intensity variation of the interrogating laser, which is recorded using an optical detector.

The output voltage at the detector further contains noise from several sources. Fig. 2 also shows the noise path, where the thermomechanical noise of the sensor, P_{TD}, transmits through the IPUT circuit. Noteworthy, the diagram only shows the transmission of P_{TD}, while other noises, such as the shot noise, are present in the optical and electric domains and are omitted from further discussion. As apparent from the figure, P_{TD} is treated as a measurement quantity by the IPUT and hence is multiplied by the RTF when it reaches the detector. Thus, to characterize P_{TD} and to obtain the RTF, we investigate the acoustic/elastic wave propagation through the IPUT.

3. Acoustic/elastic wave propagation through the IPUT sensor

Since the IPUT shown in Fig. 1 is excited by an incoming pressure pulse from a fluid medium, its wave propagation is governed by acoustic and elastic wave equations. As time-domain analysis of the IPUT in 3D at high frequencies (MHz) is computationally intensive

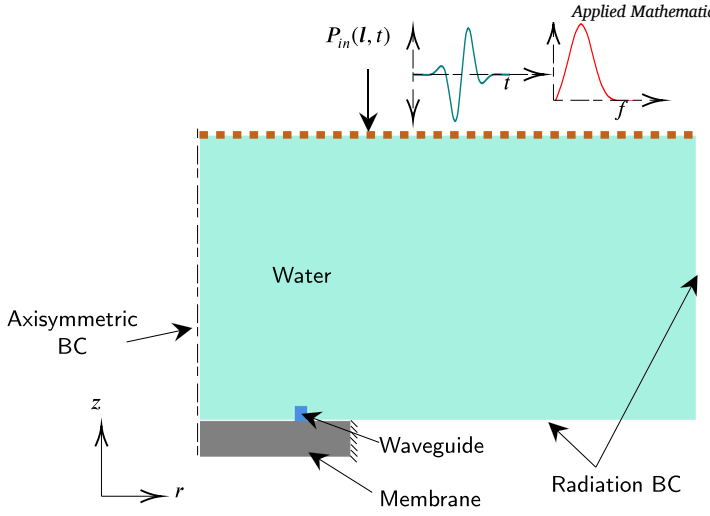

Fig. 3. Axisymmetric representation of wave propagation through IPUT when the incoming ultrasound signal is coming from water (light green region). $P(\boldsymbol{l},t)$ represents the plane Gaussian pressure pulse applied on the top edge of the water domain $\boldsymbol{l}$ marked using a brown dashed line. Radiation BCs are provided to the boundaries of the water domain to limit the reflections.

when using standard computational tools such as the finite element method (FEM), we perform the analysis in 2D axisymmetric setting. Later, we also conduct a 3D time-dependent finite element analysis of the IPUT for verification. The acoustic wave equation takes the form [41]

$$\Delta p = \rho_f \kappa \ddot{p}, \qquad \Delta \boldsymbol{v} = \rho_f \kappa \ddot{\boldsymbol{v}}, \tag{1}$$

where $p(\boldsymbol{r},t)$ and $\boldsymbol{v}(\boldsymbol{r},t)$, respectively, represent the acoustic pressure and velocity fields at the spatial coordinate $\boldsymbol{r}$ and time t. κ is the compressibility of the fluid and ρ_f is its mass density. $\Delta = \frac{\partial^2}{\partial r^2} + \frac{1}{r}\frac{\partial}{\partial r}$ is the Laplacian in a 2D axisymmetric system. Similarly, the elastic wave equation in the solid domain in the absence of damping and external source term takes the form [42],

$$\rho_s \ddot{\boldsymbol{u}} = \nabla \cdot \boldsymbol{\sigma}, \tag{2}$$

where $\boldsymbol{u} = \{u, v, w\}$ is the displacement with u, v, w, respectively, representing the displacement towards r, θ, and z directions, while ρ_s represents the density of the solid. $\boldsymbol{\sigma}$ is the Cauchy stress tensor in the solid material, whereas $\nabla\cdot$ is the vector divergence operator. For small perturbations (linear behavior) the stresses and strains within the solid domains are related by the following constitutive equation,

$$\boldsymbol{\sigma} = \boldsymbol{C} : \boldsymbol{\gamma}, \tag{3}$$

where $\boldsymbol{\gamma}$ is the strain tensor (both $\boldsymbol{\sigma}$ and $\boldsymbol{\gamma}$ are rank 2), while $\boldsymbol{C}$ is the rank 4 elasticity tensor. Since field variables are different in water and IPUT domains, we couple them using a kinematic interface condition, which ensures the continuity of normal velocity across the interface as follows,

$$\boldsymbol{n} \cdot \nabla p = -\rho_s \boldsymbol{n} \cdot \ddot{\boldsymbol{u}}, \tag{4}$$

where ∇ is the gradient operator and $\boldsymbol{n}$ is the unit outward normal vector along the interface. Additionally, we need a dynamic interface condition to ensure the continuity of the traction,

$$-p\boldsymbol{n} = \mu_s \frac{\partial \boldsymbol{u}}{\partial \boldsymbol{n}} + (\lambda_s + \mu_s)(\nabla \cdot \boldsymbol{u})\boldsymbol{n}. \tag{5}$$

The details of these interface conditions can be found in [43]. To solve this boundary value problem (BVP), it still needs necessary boundary conditions (BCs). We provide a Dirichlet BC (prescribed pressure) along the top boundary of the fluid domain as marked using a brown dashed line in Fig. 3, which takes the following form:

$$P(\boldsymbol{l},t) = \bar{P}\psi(t), \quad \text{applied at} \quad \underline{r} = \underline{l}, \tag{6}$$

where $\bar{P}$ is the constant pressure amplitude multiplied by the function $\psi(t)$ that determines the time response. The time and frequency responses of $\psi(t)$ are shown above the water domain in Fig. 3. In actual practice, the water domain is very large compared to the IPUT. To mimic this effect, we supply a plane wave radiation BC on all remaining boundaries of the fluid domain as shown in the same figure. Using Equations (1) to (6) (wave equations, interface, and boundary conditions), we can perform a time-dependent analysis of the IPUT (M) system, which provides us with instantaneous values for the independent variables (pressure, velocity, and displacement). In the next section, we describe how these variables are used to determine the RTF.

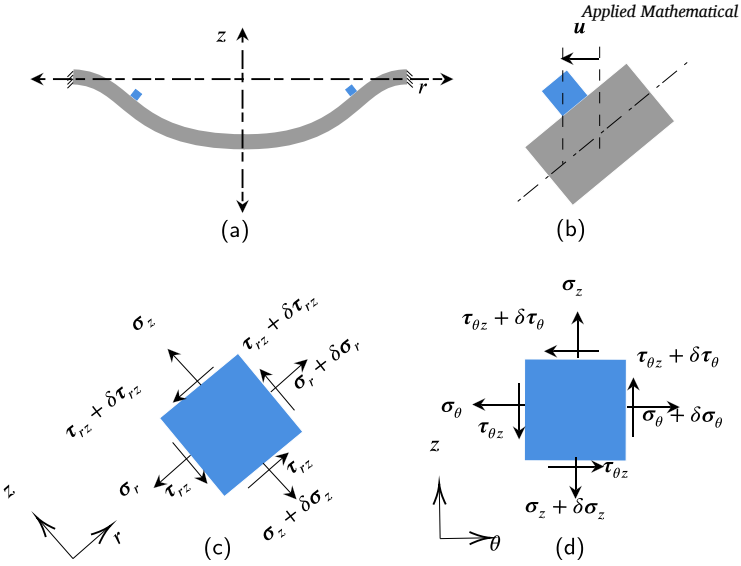

Fig. 4. Deformation of the membrane resulting in the displacement and stress of the waveguide. (a) Membrane deformed in its fundamental mode, (b) the axial displacement experienced by the waveguide due to bending of the membrane, (c) and (d), respectively, are the free body diagrams showing the normal and shear stresses in r, z and θ, z planes.

4. Receive transfer function calculation of the IPUT sensor

As shown in Fig. 2, RTF relates the incoming pressure to the wavelength/phase of the IPUT. The time-domain analysis of the IPUT (M) provides us with the displacements ($\boldsymbol{u}$) and stresses ($\boldsymbol{\sigma}$) of the waveguide. These parameters are then used to determine the IPUT's optical behavior. To that end, the following assumptions are made:

- Both the membrane and waveguide are considered thin structures, i.e., the effects of rotary inertia and shear deformation are neglected;
- Both waveguide and membrane follow linear dynamics.

Fig. 4(a) shows the behavior of the membrane-waveguide system under the influence of applied pressure. Due to the bending of the membrane, the waveguide displaces in radial and axial directions. However, since the waveguide is considered a perfect ring, to obtain its circumferential change (total length), we only need the radial displacement as marked in Fig. 4(b). In linear dynamics, the radial displacement $\boldsymbol{u}$ is directly proportional to the slope of the membrane $\frac{\partial w}{\partial r}$; thus, a higher slope yields a larger radial displacement. Figs. 4(c) and 4(d), respectively, show the stresses of the waveguide in r, z and θ, z planes due to the applied pressure. We can calculate all these displacement and stress values from the time-domain analysis discussed in the previous section. The relation between the displacements and stresses on the optical behavior is discussed next.

4.1. Wavelength change of the IPUT

The wavelength of the light traveling through the waveguide can be related to its physical length by the following expression [44]:

$$\lambda = \frac{L}{m} n_{\text{eff}}, \tag{7}$$

where λ is the optical wavelength, m is the optical mode number, L is the total length of the waveguide, and n_{eff} is the waveguide's effective refractive index, which is related to the optical wavefield. The change in the wavelength can be decomposed into changes in the refractive index and the total length as:

$$d\lambda = \frac{n_{\text{eff}}}{m} dL + \frac{L}{m}\left(dn_{\text{eff}} + \frac{\partial n_{\text{eff}}}{\partial \lambda} d\lambda\right), \tag{8}$$

where dn_{eff} is the change in the effective index of refraction due to changes of the geometry and material properties of the waveguide, but excluding the effects due to a change of wavelength. The waveguide's effective index is determined by different factors, such as the width w and height h of the waveguide, the refractive index of the material n_{mat}, and the optical resonant wavelength. We can further expand Eq. (8) as follows:

$$d\lambda - \frac{L}{m}\frac{\partial n_{\text{eff}}}{\partial \lambda} d\lambda = \frac{n_{\text{eff}}}{m} dL + \frac{L}{m}\left(\frac{\partial n_{\text{eff}}}{\partial w} dw + \frac{\partial n_{\text{eff}}}{\partial h} dh + \sum_i \frac{\partial n_{\text{eff}}}{\partial n_{\text{mat, i}}} dn_{\text{mat, i}}\right), \tag{9}$$

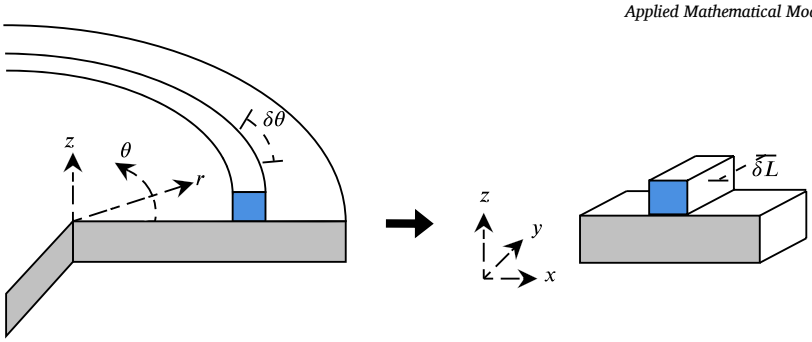

Fig. 5. Coordinate transformation between the polar and Cartesian coordinates.

substituting $n_g = \left(n_{\text{eff}} - \lambda \frac{\partial n_{\text{eff}}}{\partial \lambda}\right)$, where n_g is the group index in the above equation,

$$d\lambda = \frac{\lambda}{n_g}\left(n_{\text{eff}}\frac{dL}{L} + \frac{\partial n_{\text{eff}}}{\partial w}dw + \frac{\partial n_{\text{eff}}}{\partial h}dh + \sum_i \frac{\partial n_{\text{eff}}}{\partial n_{\text{mat, i}}}dn_{\text{mat, i}}\right). \tag{10}$$

Eq. (10) can be used to obtain the transfer function due to the radial displacement change, as follows:

$$\left(\frac{d\lambda}{dP}\right)_{\text{el}} = \frac{\lambda n_{\text{eff}} dL}{n_g L dP}, \tag{11}$$

where $dL = 2\pi u$ (u is the radial component of the displacement) is the length change due to dP, which is the change in the applied pressure. n_{eff} and n_g are obtained by the eigenvalue analysis of the optical waveguide. The influence of n_{eff} on the wavelength is more complicated since it is influenced by the geometry and material properties as shown in Eq. (10). The width and height changes are related to Poisson's effect, which can be estimated from the displacement of the waveguide using the time-domain analysis. However, the change in n_{eff} due to the change in n_{mat} is related to the photoelastic effect, which determines the effect of the induced stress (due to the incoming pressure pulse) on the refractive index of the material [45]. Since stresses are evaluated locally, we need to transform the coordinate system from polar to Cartesian to determine the photoelastic tensor.

4.2. Coordinate transformation

A ring waveguide sitting on a circular membrane in the polar coordinate system is shown in the left part of Fig. 5. When analyzing the system locally, for an infinitesimal angle $\delta\theta$, the waveguide element can be approached as a straight waveguide with infinitesimal length δL in Cartesian coordinates, as shown on the right side of the same figure. This allows us to make the following assumptions. The stresses and strains in the r direction (σ_r and ϵ_r) can be approximated by those in the x direction (σ_x and ϵ_x). Simultaneously, σ_θ and ϵ_θ are equivalent to σ_y and ϵ_y, while σ_z and ϵ_z are same in both coordinate systems. With these assumptions, we proceed to evaluate the photoelastic effect as described below.

4.3. Photoelastic effect of the IPUT

Light propagating through an optical waveguide is governed by Maxwell's equations. With the absence of a source term, the equations take the form [46]:

$$\nabla \times \tilde{E} = -\mu\frac{\partial \tilde{H}}{\partial t}, \qquad \nabla \times \tilde{H} = \epsilon\frac{\partial \tilde{E}}{\partial t}, \tag{12}$$

where $\tilde{E}$ and $\tilde{H}$, respectively, are the electric and magnetic fields, μ is the permeability and ϵ is the permittivity of the medium. The permittivity or dielectric tensor in 3D takes the following form [47]:

$$\epsilon = \begin{bmatrix} n_{xx}^2 & n_{xy}^2 & n_{xz}^2 \\ n_{xy}^2 & n_{yy}^2 & n_{yz}^2 \\ n_{xz}^2 & n_{yz}^2 & n_{zz}^2 \end{bmatrix}, \tag{13}$$

where n_{ij} for $i, j \in \{x, y, z\}$ are refractive indices. Due to loading (internally or externally), stresses develop within the waveguide resulting in changes in these refractive indices, which phenomenon is known as the photoelastic effect. Photoelastic coefficients for silicon and other common materials have been calculated in literature [48]; however, they are still incomplete, and we do not have all components of the anisotropic photoelastic tensor. The literature only reports the values for strain-optics constants p_{11} and p_{12}. Thus, the relation between the refractive index, $\boldsymbol{n}$, and strain $\boldsymbol{\gamma}$ for an isotropic point group is used, which can be expressed as [49]

$$\begin{Bmatrix} 1/n_{xx}^2 \\ 1/n_{yy}^2 \\ 1/n_{zz}^2 \\ 1/n_{yz}^2 \\ 1/n_{xz}^2 \\ 1/n_{xy}^2 \end{Bmatrix} = \begin{Bmatrix} 1/n_0^2 \\ 1/n_0^2 \\ 1/n_0^2 \\ 0 \\ 0 \\ 0 \end{Bmatrix} - \begin{bmatrix} p_{11} & p_{12} & p_{12} & 0 & 0 & 0 \\ p_{12} & p_{11} & p_{12} & 0 & 0 & 0 \\ p_{12} & p_{12} & p_{11} & 0 & 0 & 0 \\ 0 & 0 & 0 & p_{44} & 0 & 0 \\ 0 & 0 & 0 & 0 & p_{44} & 0 \\ 0 & 0 & 0 & 0 & 0 & p_{44} \end{bmatrix} \begin{Bmatrix} \gamma_{xx} \\ \gamma_{yy} \\ \gamma_{zz} \\ \gamma_{yz} \\ \gamma_{xz} \\ \gamma_{xy} \end{Bmatrix}, \tag{14}$$

where $p_{44} = \frac{1}{2}(p_{11} - p_{12})$ and n_0 is the isotropic refractive index. This relation can be expressed in terms of stresses by using the constitutive relations:

$$\boldsymbol{n}_{ij} = \boldsymbol{n}_0 - \boldsymbol{C}_m \boldsymbol{\sigma}_{ij}, \tag{15}$$

where $\boldsymbol{C_m}$ for $m \in \{1,2,3\}$ are the stress-optic constants whose values can be obtained by the following expressions,

$$C_1 = n_0^3 \left(p_{11} - 2\nu p_{12}\right)/2E \qquad C_2 = n_0^3 \left[p_{12} - \nu \left(p_{11} - p_{12}\right)\right]/2E \qquad C_3 = n_0^3 p_{44}/2G \tag{16}$$

where E is the Young's modulus, ν is the Poisson's ratio, and G is the shear modulus.

The stress values from the time-domain acoustic analysis can be used in Eq. (15) to obtain the variations in the refractive index of the waveguide material(s). This new refractive index can then be used to solve the Maxwell equations (Eq. (12)) to derive the n_{eff} of the waveguide for the supplied geometry. The variations in the n_{eff} produce a wavelength shift of the waveguide as per Eq. (10). The resulting transfer function can be expressed as follows:

$$\left(\frac{d\lambda}{dP}\right)_{\text{ref}} = \frac{\lambda}{n_g}\frac{dn_{\text{eff}}}{dP}. \tag{17}$$

Thus, the IPUT's RTF due to the incoming pressure wave is the combination of the RTF due to elongation and photoelastic effect, which can be expressed as:

$$\left(\frac{d\lambda}{dP}\right) = \left(\frac{d\lambda}{dP}\right)_{\text{el}} + \left(\frac{d\lambda}{dP}\right)_{\text{ref}} = \frac{\lambda}{n_g L}\left(n_{\text{eff}}\frac{dL}{dP} + L\frac{dn_{\text{eff}}}{dP}\right). \tag{18}$$

Notably, wavelength changes brought on by variations in the cross-sectional geometry of the waveguide and the vacuum wavelength have far less of an impact and are not taken into account in the model [50].

5. Noise equivalent pressure of the IPUT sensor

The NEP of the IPUT (or any transducer) can be generally defined using the following expression:

$$NEP = p_N / RTF, \tag{19}$$

where p_N is the measured noise pressure. The NEP corresponds to the minimum detectable pressure where the pressure amplitude is 1σ (σ standard deviation) noise level. In the following, we derive the expression for the noise equivalent pressure generated by the thermal noise (NEP_T).

Thermal noise is generated by losses in the sensor and Brownian motion in the surrounding medium [51]. The thermal noise contribution in the output response is derived as Nyquist noise [52], while also incorporating complex geometric features and multiple materials. The following assumptions are used in addition to the ones discussed in Section 4:

- The excitation of the membrane is only via the thermal displacement of the membrane, i.e., no other source term is present in the system;
- The motion of the membrane is assumed to follow the behavior of a weakly damped single harmonic oscillator (see Fig. 6(b));

The following considerations are also made to incorporate the influence of the surrounding fluid medium on the IPUT:

- The inertia effect of the fluid load is incorporated in the effective mass of the resonator;
- The resonator's damping factor includes the dissipation due to the acoustic radiation to the fluid;
- The resonator's effective stiffness incorporates the fluid's influence on the resonance frequency.

According to the equipartition theorem, the energy is shared equally amongst all energetically accessible degrees of freedom (DOFs), and each quadratic DOF will, on average, possess an energy of $\frac{1}{2}k_B T$, where k_B is the Boltzmann's constant whose value in SI unit is 1.38×10^{-23} J/K and T is the absolute temperature in Kelvin. In the case of the micro-mechanical resonator, we use a displacement DOF, $\boldsymbol{U}$ to represent its motion, which in a linear regime can be expressed as the product of spatial and temporal functions.

$$\boldsymbol{U}(\boldsymbol{x}, t) = \phi(t)\bar{\boldsymbol{u}}(\boldsymbol{x}), \tag{20}$$

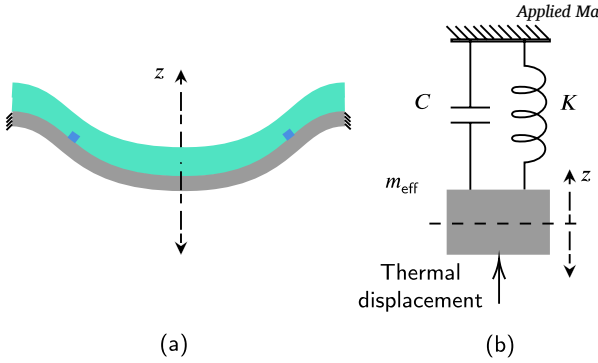

Fig. 6. IPUT with the surrounding fluid represented as a single harmonic oscillator (a) Membrane deformation (with the fluid on top) dominated by its fundamental mode, (b) Motion of the IPUT in the presence of surrounding fluid medium represented as a weakly damped single harmonic oscillator with K stiffness, C damping factor, and m_{eff} the effective mass of the oscillator. The thermal displacement from the fluid acts as the source term for the membrane.

where $\bar{\boldsymbol{u}}$ is the mode shape corresponding to the desired motion of the membrane, while ϕ is the time-dependent function describing the membrane's motion. The mode shape can be computed by the eigenvalue analysis of the membrane, which, depending on the complexity of the geometry, can be performed analytically or numerically. $\phi(t)$ can be obtained by solving the differential equation of motion (DEOM) of the membrane. For simplicity, we represent the IPUT membrane as a single harmonic oscillator with stiffness K, damping factor C, and the effective mass m_{eff} as shown in Fig. 6. The DEOM then can be represented as follows:

$$m_{\text{eff}}\ddot{\phi} + C\dot{\phi} + K\phi = F(t). \tag{21}$$

Here m_{eff} incorporates the influence of the fluid and can be expressed as follows [53]:

$$m_{\text{eff}} = (1+\beta)m_s \tag{22}$$

where m_s is the mass of the sensor and $\beta = 0.65381\frac{\rho_f \times r_s}{\rho_s \times t_s}$ is the fluid mass contribution factor [54]. $F(t)$ is the applied force, which can be expressed as the product of the applied pressure $p(t)$ and the cross-sectional area A_s. The NEP_T for the resonator is the ratio of the resonator's spectral response due to the thermal Langevin force divided by the pressure sensitivity of the resonator [55]. The Langevin force represents the fluctuating part of the Brownian motion, which acts as the source term for the resonator's motion. Since the generated thermal noise is a Gaussian white noise, it can be separated into different frequency components (spectral response). The sensitivity of the resonator due to the applied pressure can be obtained by solving Eq. (21) in the frequency domain and dividing it by the input pressure (also in the frequency domain) [56]:

$$\Sigma(\omega) = \Phi(\omega)/P(\omega), \tag{23}$$

where $\Sigma(\omega)$ is the sensitivity expressed in m/Pa. Here $\Phi(\omega)$ and $P(\omega)$, respectively, are Fourier transforms of the displacement, $\phi(t)$, and pressure $p(t)$. To obtain the resonator's response due to thermal force by the equipartition theorem, we need to express the mean-square amplitude of motion in terms of the power spectral density (PSD). The PSD is obtained by squaring the frequency spectrum of the resonator's motion ($\Phi(\omega)$) and dividing it by the resolution bandwidth (RBW—the frequency range of the resonator's response bounded by -6 dB signal amplitude). To obtain the PSD, an autocorrelation function $R(t)$ is used, which relates the signal amplitude to itself at a later time [56].

$$R(t) = \lim_{T_0\to\infty} \frac{1}{T_0}\int_0^{T_0} \phi(t')\phi(t'+t)dt', \tag{24}$$

where T_0 is the time window. The two-sided PSD, $\tilde{P}(\omega)$, is the Fourier transform of the autocorrelation function [57]. Similarly, $R(t)$ is the inverse Fourier transform of $\tilde{P}(\omega)$.

$$\tilde{P}(\omega) = \int_{-\infty}^{\infty} e^{i\omega t}R(t)dt \qquad R(t) = \frac{1}{2\pi}\int_{-\infty}^{\infty} e^{-i\omega t}\tilde{P}(\omega)d\omega. \tag{25}$$

In real situations, $\tilde{P}(\omega)$ is an even function and thus can be expressed using the positive frequency range such that the single-sided PSD, $S(\omega) = 2\tilde{P}(\omega)$ [58]. The mean-square amplitude of the motion is defined as:

$$\langle\phi^2(t)\rangle = \frac{1}{T_0}\int_0^{T_0} [\phi(t)]^2 dt, \tag{26}$$

which is identical to $R(t)$ at zero time shift provided the signal is sampled for a sufficiently long time window. Using Eq. (25), $\langle a^2(t)\rangle$ can be expressed in terms of the PSD [59].

$$\langle \phi^2(t)\rangle = \frac{1}{2\pi}\int_0^\infty S(\omega)d\omega. \tag{27}$$

By taking the Fourier transform of Eq. (21), we can express $S(\omega)$ in terms of $S_F(\omega)$, which is the PSD due to the forcing function $F(t)$:

$$S(\omega) = |\chi|^2 S_F(\omega), \tag{28}$$

where χ is the mechanical susceptibility obtained as [37]:

$$\chi(\omega) = \frac{\mathcal{F}(\phi(t))}{\mathcal{F}(F(t))} = \frac{1}{m_{\text{eff}}(\omega_0^2 - \omega^2 + i\omega\omega_0/Q)^{0.5}}, \tag{29}$$

where ω_0 and Q are the natural frequency and the Q-factor of the resonator (corresponding to the required mode). Since $F(t)$ is generated by the thermal noise, which is broadband, $S_F(\omega)$ can be considered to be a constant thermal force S_F^T. By using Equations (27) to (29), we can write:

$$\langle \phi^2(t)\rangle = \frac{S_F^T}{2\pi m_{\text{eff}}^2}\int_0^\infty \frac{d\omega}{(\omega^2-\omega_0^2)^2 + (\omega\omega_0/Q)^2} = \frac{S_F^T Q}{4\omega_0^3 m_{\text{eff}}^2}. \tag{30}$$

Using the equipartition theorem, we represent the time-averaged potential energy $\tilde{U}$ of the resonator as follows:

$$\langle \tilde{U}\rangle = \frac{1}{2}m_{\text{eff}}\omega_0^2\langle\phi^2(t)\rangle = \frac{1}{2}k_B T. \tag{31}$$

From Eqs. (30) and (31), we get the expression of S_F^T as:

$$S_F^T = \frac{4k_B T\omega_0 m_{\text{eff}}}{Q}, \tag{32}$$

and the resonator's PSD as:

$$S(\omega) = \frac{4k_B T\omega_0}{m_{\text{eff}}Q[(\omega-\omega_0)^2 + (\omega\omega_0/Q)^2]}. \tag{33}$$

As mentioned previously, to get the NEP, we also need to obtain the pressure sensitivity ($\Sigma(\omega)$) of the resonator. $\Sigma(\omega)$ can be obtained by using the mechanical susceptibility (refer Eq. (29)) as follows [35]:

$$\Sigma(\omega) = \frac{A_s}{m_{\text{eff}}[(\omega^2-\omega_0^2)^2 + (\omega\omega_0/Q)^2]^{0.5}}, \tag{34}$$

where A_s is the cross-sectional area of the sensor. Now, from Eqs. (33) and (34), we obtain thermal-noise-induced pressure of the sensor as follows:

$$p_s = \frac{\sqrt{S}}{\Sigma} = \sqrt{\frac{4k_B T\omega_0 m_{\text{eff}}}{QA_s^2}} \tag{35}$$

As shown in Fig. 2 and Section 2, p_s gets multiplied by the RTF (Eq. (18)) at the receiver. Hence, the equivalent of p_s in wavelength (NEP_λ) or phase (NEP_ϕ) is used to represent the thermal noise as follows:

$$NEP_{\lambda s} = \left(\frac{d\lambda}{dP}\right)p_s = \frac{\lambda}{n_g L}\left(n_{\text{eff}}\frac{dL}{dP} + L\frac{dn_{\text{eff}}}{dP}\right)\sqrt{\frac{4k_B T\omega_0 m_{\text{eff}}}{QA_s^2}}. \tag{36}$$

To minimize p_s, we need to maximize Q and A_s while minimizing m_{eff}, and ω_0 of the membrane. In the case of medical ultrasound imaging, the penetration depth decides the required central frequency, and the axial resolution of the image dictates the frequency bandwidth; hence, these parameters cannot be modified to improve p_s. The remaining parameters m_{eff} and A_s are also not independent; for instance, increasing A_s (without changing the thickness) would increase m_{eff}, but also decreases ω_0 and the bandwidth. To study the sensor's performance under various parameters, we investigate the influence of variations in geometry and material properties on p_s. These effects are incorporated via m_{eff}.

5.1. Incorporating complex geometric and material behavior via the effective mass

The effective mass of each resonator mode can be obtained from its potential energy. For the n^{th} mode, each volume element dV will have a potential energy corresponding to the harmonic oscillator with a mass element $dm = \rho(\boldsymbol{x})dV$ given by:

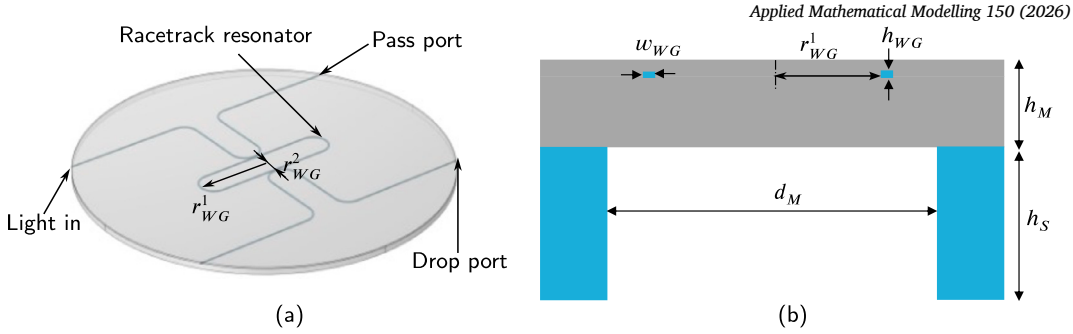

Fig. 7. The IPUT design from [60] where (a) is the isometric view and (b) shows the side view of the IPUT only considering the racetrack waveguide (excluding all ports) with the substrate backing. Here the waveguide width $w_{\mathrm{WG}} = 400\,\mathrm{nm}$, its height $h_{\mathrm{WG}} = 220\,\mathrm{nm}$, the diameter of the membrane $d_M = 124\,\mu\mathrm{m}$, its height $h_M = 2.5\,\mu\mathrm{m}$, and the height of the substrate $h_S = 250\,\mu\mathrm{m}$. The major radius of the racetrack is $r^1_{\mathrm{WG}} = 18\,\mu\mathrm{m}$ while its minor radius is $r^2_{\mathrm{WG}} = 5\,\mu\mathrm{m}$. The input (laser coming in), pass, and drop ports are also marked in (a).

$$d\tilde{U} = \frac{1}{2}\rho(\boldsymbol{x})\omega_n^2|\phi_n(t)\boldsymbol{u}_n(\boldsymbol{x})|^2 dV \tag{37}$$

The total potential energy of the mode is given by integrating over the entire volume of the device, V.

$$\tilde{U} = \frac{1}{2}\omega_n^2|\phi_n(t)|^2 \int \rho(\boldsymbol{x})|\boldsymbol{u}_n(\boldsymbol{x})|^2 dV = \frac{1}{2}\omega_n^2|\phi_n(t)|^2 m_{eff}, \tag{38}$$

where m_{eff} is defined as:

$$m_{\mathrm{eff}} = \int \rho(\boldsymbol{x})|\boldsymbol{u}_n(\boldsymbol{x})|^2 dV. \tag{39}$$

Thus, with the normalized mode shape $\boldsymbol{u}_n(\boldsymbol{x})$, m_{eff} can be calculated. We can numerically obtain the normalized mode for a complex geometry (e.g., via FEM), which can be used to determine its effective mass. Additionally, the density, ρ is also a function of space; thus, multiple layers can also be included in the membrane aiding us in exploring different possibilities to minimize NEP_T.

Note that the expression of NEP (Equations (35)) is in terms of $\mathrm{Pa}/\sqrt{\mathrm{Hz}}$, which needed to be multiplied by the square root of the operation bandwidth to obtain the NEP in Pa. The expressions of RTF and NEP complete the IPUT model, and we proceed to the model validation.

6. Validation of RTF and NEP models

To validate the RTF and NEP models, we compare various properties of the IPUT namely, the resonance frequency, Q-factor, RTF, and NEP, with the literature. To that end, we select the design discussed in [15,60], shown in Fig. 7. The membrane is composed of SiO_2 with density $\rho_m = 2200\,\mathrm{kg/m^3}$, elastic modulus $E_m = 70\,\mathrm{GPa}$, and Poisson ratio 0.17, and has a diameter of 124 µm and a thickness of 2 µm. The racetrack waveguide is made of silicon with density $\rho_{\mathrm{WG}} = 2329\,\mathrm{kg/m^3}$, elastic modulus $E_{\mathrm{WG}} = 165\,\mathrm{GPa}$, and Poisson ratio 0.28, and has a width of 400 nm and a height of 220 nm. The waveguide is attached to the membrane, which has the major radius of $r^1_{\mathrm{WG}} = 18\,\mu\mathrm{m}$ and minor radius of $r^2_{\mathrm{WG}} = 5\,\mu\mathrm{m}$. A SiO_2 cladding of 0.5 µm is then provided on top to protect the waveguide from the environment. Thus, the total thickness of the membrane is 2.5 µm.

6.1. Elasto-acoustic solver settings

The wave propagation analysis discussed in Section 3 is performed using a time-domain FEM solver provided by Comsol. Here we have employed an implicit (backward Euler method) solver where time integration is carried out via generalized alpha [61]. This method is the generalization of the Newmark method of time integration, which gives an optimized way of adding high-frequency dissipation to a finite element transient dynamic simulation. In the model, the solid mechanics module is used for the IPUT domain, while the water domain is modeled via the pressure acoustics time domain module. An acoustic-structure interaction interface ensures the satisfaction of the interfacial conditions described in Equations (4) and (5). A plane pressure pulse of 10 kPa amplitude with a central frequency of f_c and 80 % −6 dB BW is applied on top of the fluid domain as described in Fig. 3. Since the size of the fluid domain is much larger than the IPUT, the supplied pulse can be considered as a plane wave without focusing or diffraction effects. The time-domain analysis for 40 cycles is performed with a time step of T/15. T is the period corresponding to $f_{\max} = 2f_c$.

6.2. Time- and frequency-domain behavior of the IPUT

The surface displacement of the IPUT corresponding to the peak axial displacement (in time) is plotted in Fig. 8(a), whereas the fundamental eigenmode of the IPUT (without the presence of fluid) with clamped BC is shown in Fig. 8(b). Comparing these two plots, we can infer that the IPUT's dynamic response is dominated by its fundamental mode, and our single-harmonic oscillator assumption holds. We then study the time-domain response.

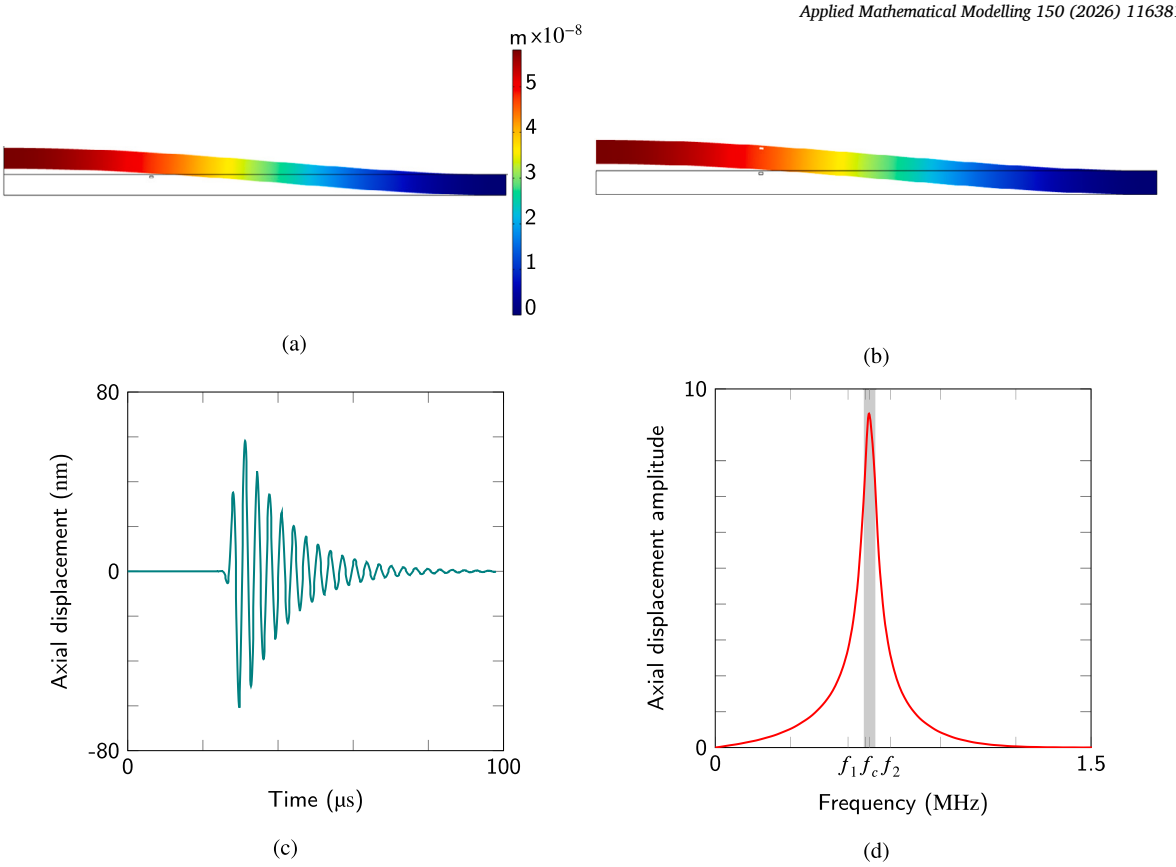

Fig. 8. (a) The axial displacement profile of the IPUT corresponding to the peak displacement (in time). (b) The fundamental mode shape of the IPUT was obtained from a standard eigenvalue analysis of the IPUT without water. The output displacement signal is represented as a function of (c) time and (d) frequency. The frequencies that correspond to the peak displacement ($f_c = 0.615\,\text{MHz}$), and the lower ($f_1 = 0.59\,\text{MHz}$) and upper ($f_2 = 0.642\,\text{MHz}$) bounds of -3 dB BW are also marked in (b).

The axial displacement of the membrane extracted at its center is plotted in Fig. 8(c), which behaves similarly to a damped harmonic oscillator. The frequency response is obtained by transforming the time response to the frequency domain via the Fourier transform (FFT) as shown in Fig. 8(d). Here the -3 dB bandwidth (BW), also called full-width half maximum (FWHM), is shown using a gray-shaded box bounded by $f_1 = 0.59\,\text{MHz}$ and $f_2 = 0.642\,\text{MHz}$. The frequency corresponding to the peak displacement provides its resonant frequency, which is $f_c = 0.615\,\text{MHz}$. The experimentally obtained resonance frequency from [15] is 0.76 MHz, which is about 19 % higher than the numerical predictions. This difference is due to the geometric variations during the fabrication (diameter and thickness change due to over/under etching of the membrane) and the effect of prestress as discussed in [22]. We calculate the Q-factor from this frequency response using the Lorentzian as follows:

$$Q = \frac{f_c}{f_2 - f_1} = 11.75, \tag{40}$$

resulting in a -3 dB BW of 8.5 %. The Q-factor obtained experimentally is around 10 [60], which is 15 % lower than the model prediction. We further estimate the output transfer function of the IPUT by using the displacement of the waveguide as discussed next.

6.3. Receive transfer function of the IPUT

Since the exerted pressure deforms the waveguide along with the membrane, we calculate the RTF of the IPUT due to the wavelength change and the photoelastic effect as discussed in Section 4. To obtain the wavelength change, we need to determine the waveguide's physical length change, which is influenced by its radial displacement. The radial displacement as a function of time (similar to Fig. 8(c)) is extracted along the thickness of the waveguide (see the inset of Fig. 9). These time responses are then transformed into the frequency domain (like Fig. 8(d)) from which the displacements corresponding to the resonant frequency f_c are selected and plotted against the distance from the bottom of the waveguide (through its height) as shown in Fig. 9. Using this radial displacement, we obtain the RTF. To that end, n_{eff} and n_g are needed, while ΔP is the incoming pressure value corresponding to the resonant frequency (taken from the input pulse) and $\lambda = 1550\,\text{nm}$ is the optical wavelength. n_{eff} and n_g are calculated using FIMMWAVE [62] as discussed in the next section.

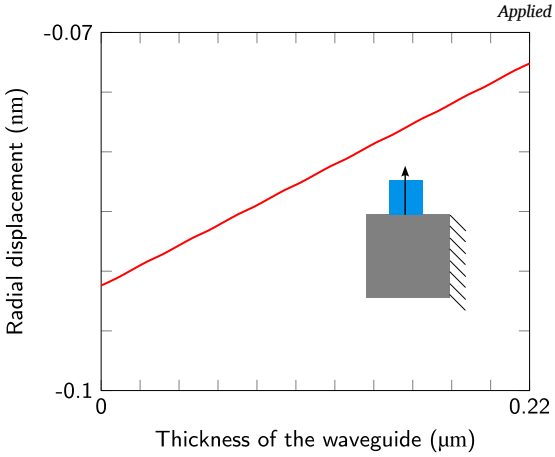

Fig. 9. Radial displacement extracted along the thickness of the waveguide. The inset shows the schematic of the waveguide and membrane region where the arrow goes through the center of the waveguide and represents the abscissa.

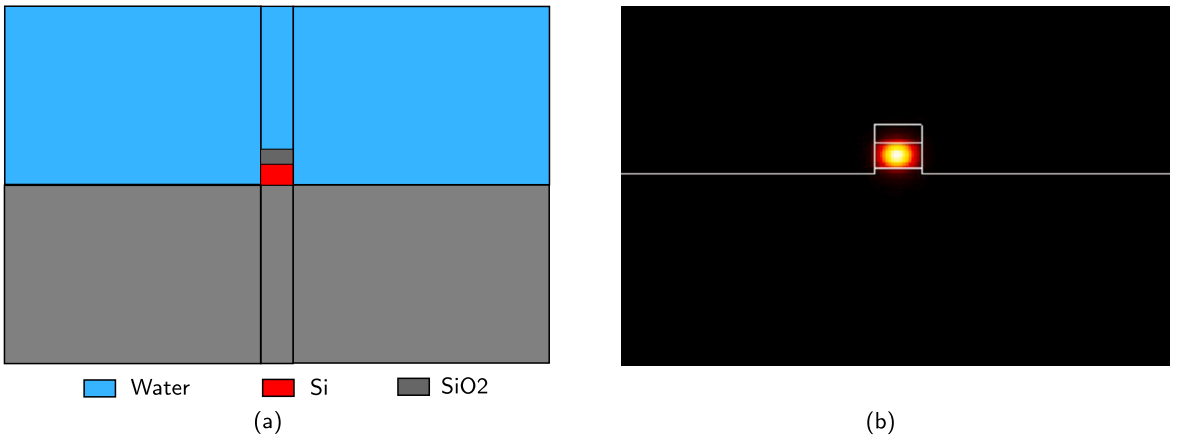

Fig. 10. Optical mode shape calculation using FIMMWAVE from Photon Design. (a) The graphical interface where the cross-section of the optical waveguide (Si) and cladding (SiO_2 and water) layers are defined. (b) Corresponding fundamental TE mode resulting in $n_{\text{eff}} = 2.228$ and $n_g = 4.386$.

6.4. Optical analysis

Optical analysis is performed using Photon Design's FIMMWAVE, which is an optical analysis tool containing both semi-analytical and numerical solvers [62]. For the domain with a uniform geometry such as ours (rectangular waveguide), the semi-analytical method based on a fully vectorial film model matching (FMM) solver is adequate. The method does not require discretization and is therefore computationally inexpensive for modeling waveguides. Additionally, the solver supports various configurations, including transverse electric (TE), transverse magnetic (TM), and mixed modes.

The cross-sectional view of the IPUT with its surrounding medium (water) is shown in Fig. 10(a), whose eigenvalue analysis is performed using FIMMWAVE. Since optical waves travel much faster than ultrasound, we assume a static response for the optical portion of the IPUT. By solving Maxwell's equations, we obtain the eigenmode (the fundamental mode with TE polarization is shown in 10(b)). The corresponding effective and group indices are obtained as $n_{\text{eff}} = 2.228$ and $n_g = 4.386$. The optical wavelength $\lambda = 1550\,\text{nm}$ is taken identical to the experimental setup discussed in [15].

By using Eq. (11), we calculate the RTF due to the wavelength shift as $\left(\frac{\Delta\lambda}{\Delta P}\right)_{\text{el}} = -27\,\text{fm/Pa}$. RTF of the IPUT due to stresses is more complicated, since the stresses are rank 2 tensors as opposed to displacements (vectors). Additionally, the waveguide is defined in the cylindrical coordinate system (refer Figs. 4(c) and 4(d)) while the photoelastic tensor is in the Cartesian coordinate system (see Eq. (14)), so as discussed in Section 4.2, we transform the waveguide from polar to Cartesian coordinates as shown in Fig. 5. The stresses towards r (radial), θ (angular), and z (axial) directions are then used, respectively, as stresses in x, y, and z directions. The resulting relationship between different normal stresses and the thickness of the waveguide is provided in Fig. 11. The shear stresses were negligible compared to the normal stresses and, therefore, were omitted. Additionally, the axial stress (σ_z) is approximately two orders of magnitude lower than the angular and radial stresses. Hence, the effect of Poisson's ratio on the wavelength shift would also be lower. Using the stress values and the photoelastic tensor from Eq. (14), we can calculate the transfer function due to the stresses using Eq. (17). Here $C_1 = -1.25 \times 10^{-11}\,\text{Pa}^{-1}$ and $C_2 = 4.66 \times 10^{-12}\,\text{Pa}^{-1}$ are selected for silicon [48] and resulting wavelength shift

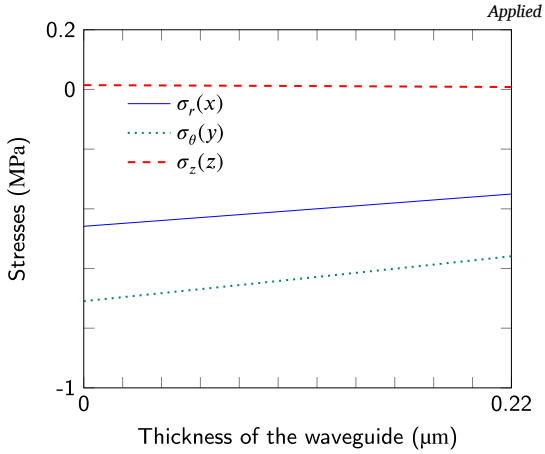

Fig. 11. Normal stresses on the waveguide measured along the vertical edge of the waveguide. (a) coordinate transformation from cylindrical to Cartesian coordinate system and (b) corresponding stresses extracted along the waveguide thickness, where the axial stress is acting in the opposite direction and has a considerably lower magnitude than radial and angular values.

due to the stress is $\left(\frac{\Delta\lambda}{\Delta P}\right)_{\text{ref}} = -6.53\,\text{fm/Pa}$. Thus, the total RTF of IPUT due to elongation and photoelasticity is $-33.6\,\text{fm/Pa}$. The total wavelength shift obtained experimentally in [60] is 67 fm/Pa, which is twice the model prediction. This could be due to the effects of geometric variation during fabrication (for instance, a change in membrane thickness by over-etching) and the prestress.

6.5. Comparison of the IPUT's RTF with a 3D model

Since the IPUT geometry provided in Fig. 7(a) is not of an axisymmetric device, we also check its response using a 3D acousto-mechanical model. The 3D analysis is very similar to the 2D axisymmetric modeling discussed in Section 3, except that waves propagating in all directions are considered and the BCs are modified. Here, instead of an axisymmetric BC, symmetric BCs are provided to the solid domain (two flat surfaces) and fluid domain (four flat surfaces normal to the x, y plane) as shown in Fig. 12. The time-domain analysis is performed for 40 cycles with a time step of T/15 (similar to the axisymmetric model). The resulting time and frequency response of the axial displacement are provided in Figs. 13(a), and 13(b), respectively. Since the dynamic response of the IPUT is dominated by the membrane, its resonance frequency and Q factor are comparable with the 2D axisymmetric analysis and we observe that the resonance frequency is 0.623 MHz (1.3 % higher than corresponding 2D axisymmetric case) while the Q-factor is 11.5 (2.2 % lower than 2D axisymmetric case). The RTF is calculated by using the radial displacement of the waveguide shown in Fig. 14(a) for which the quarter racetrack is used (see the inset of Fig. 14(a)). The displacement is then multiplied by four to get the total radial expansion of the ring. Similarly, the stresses are also calculated along the waveguide's height as shown in Fig. 14(b), which is used to obtain the variations in n_{eff}. The RTF obtained from the 3D model by combining both elongation $\left(\frac{\Delta\lambda}{\Delta P}\right)_{\text{el}} = -19\,\text{fm/Pa}$ and photoelastic effects $\left(\frac{\Delta\lambda}{\Delta P}\right)_{\text{ref}} = -3\,\text{fm/Pa}$ is $-22\,\text{fm/Pa}$ at 0.623 MHz. Although the resonance frequency and Q-factor are comparable between the 3D and 2D axisymmetric models, the RTF obtained here is about 35 % lower than the 2D axisymmetric case. This is because, in the former, the actual racetrack geometry of the optical ring characterized by R^1_{WG} and R^2_{WG} from Fig. 7(a) is considered, while in the latter, a circular ring with the radius same as R^1_{WG} of the racetrack is used (see Fig. 7(b)). This leads to a larger length change in the waveguide and thereby higher RTF in the case of the 2D axisymmetric analysis. Nevertheless, both 2D axisymmetric and 3D analysis predicts lower RTF values (factor of 2 for 2D and 3 for 3D) than those of the experiments, which could be due to the influence of prestress on the IPUT.

6.6. Comparison between static and dynamic IPUT models

The static model to determine the parameters of IPUT is discussed in [16,19] where the IPUT is assumed to undergo static deflection due to the incoming pressure. The phase change ($\Delta\phi$) due to the incoming pressure p is written as follows [19]:

$$\Delta\phi = \frac{4\pi^2}{\lambda} n_{\text{eff}} \frac{4R_{\text{WG}}Z_{\text{WG}}}{R^2}\left(1 - \frac{R^2_{\text{WG}}}{R^2}\right) w_0, \tag{41}$$

where R_{WG} and Z_{WG} are the coordinates of the waveguide and R is the radius of the membrane. $w_0 = \frac{\Delta p R^4}{64D}$ is the static deflection of the axial center of the membrane with $D = \frac{Eh^3}{12(1-\nu^2)}$ being the flexural rigidity [19]. Here h is the thickness of the membrane. Substituting the values of w_0 and D into Equation (41), we get the phase transfer function as:

$$\frac{\Delta\phi}{\Delta p} = \frac{3\pi^2 n_{\text{eff}}}{\lambda} \frac{Z_{\text{WG}}}{h^3} \frac{(1-\nu^2)}{E}\left(R^2 - R^2_{\text{WG}}\right) R_{\text{WG}}. \tag{42}$$

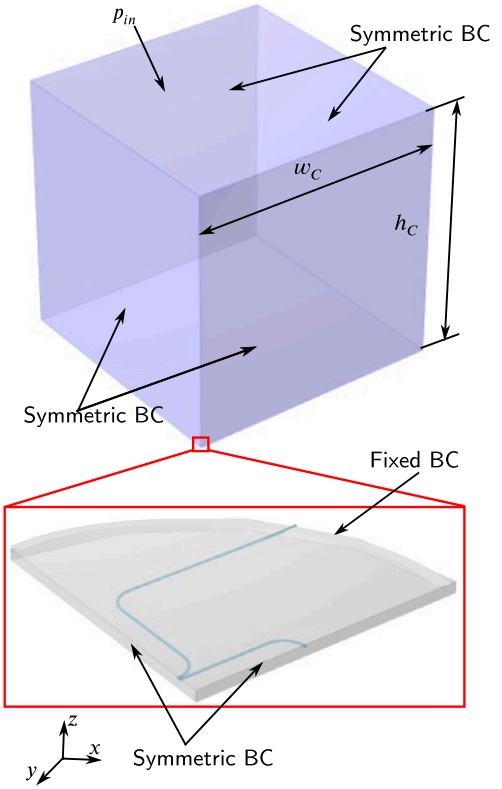

Fig. 12. Schematic representation of the 3D IPUT model, where the blue region represents the fluid domain while the gray and teal (embedded in gray) regions, respectively, are the membrane and waveguide. Since the RR is quarter-symmetric, symmetry BCs are provided on the two flat surfaces of the membrane and waveguide system. Additionally, for the fluid domain, symmetric BCs are supplied on all flat surfaces perpendicular to the x, y plane, while the top surface is provided with a prescribed pressure (P_{in}) load, and the bottom surface is left free. The width of the fluid domain is $w_C = 6.25$ mm while the height $h_C = 25$ mm.

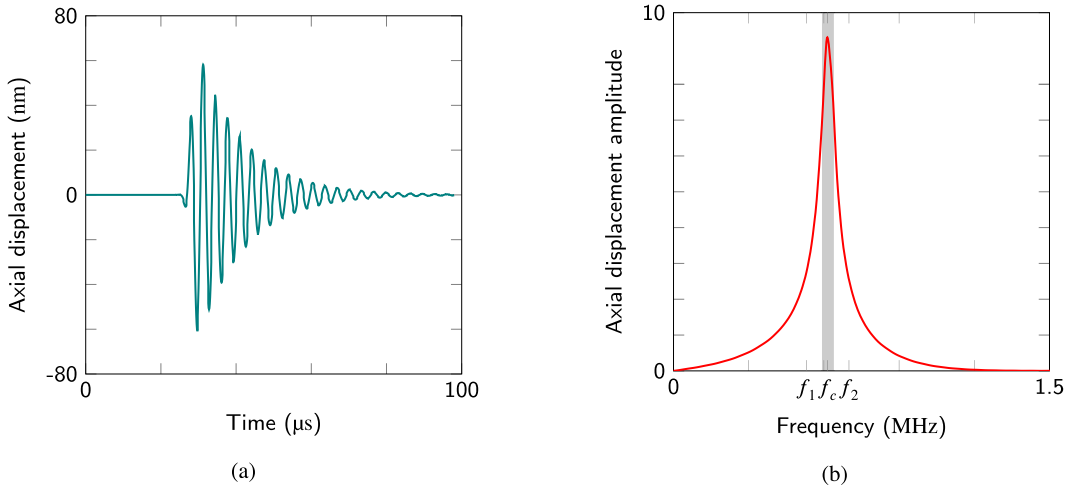

Fig. 13. The output displacement signal computed for the 3D model is represented as functions of (a) time and (b) frequency. The frequencies correspond to the peak displacement ($f_c^* = 0.623$ MHz), the lower ($f_1^* = 0.594$ MHz) and upper ($f_2^* = 0.648$ MHz) bounds of the −3 dB BW are also marked in (b). See Fig. 8(d) for corresponding values in 2D axisymmetric case.

Using the relation between the phase and length change (Δl) of the waveguide, $\Delta\phi = \frac{2\pi n}{\lambda}\Delta l$ and the relation between the length change and wavelength change from Equation (11), we can modify the above equation to the expression for RTF as follows:

$$\frac{\Delta\lambda}{\Delta p} = \frac{3\pi n_{\text{eff}}\lambda}{2n_g L}\frac{(1-\nu^2)}{E}\left(R^2 - R_{\text{WG}}^2\right)R_{\text{WG}}. \tag{43}$$

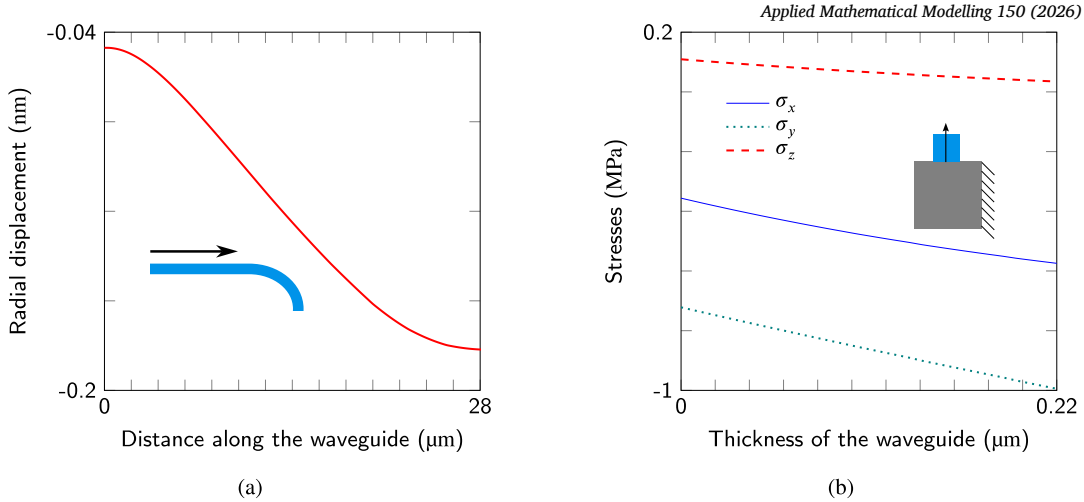

Fig. 14. (a) Radial displacement extracted along the waveguide. The inset shows the schematic of the quarter waveguide where the arrow represents the direction along which the displacement is extracted. (b) Different stresses of the waveguide extracted along its thickness (the inset shows the schematic of the region of the waveguide and membrane).

After substituting the material and geometric parameters from Section 6, we obtain the RTF as $\frac{\Delta\lambda}{\Delta P} = 1.6\,\mathrm{fm/Pa}$, which is 41 times lower than the experimental value (67 fm/Pa), while the RTF predicted by our dynamic model is only two times lower than the experiment (33 fm/Pa). This discrepancy between the two models (a factor of 20) is mainly due to the influence of the dynamic response (taken care of by the Q factor of 12) and the effects of prestress (as discussed in the subsequent section). Thus, we can infer that a dynamic model is essential to accurately determine the IPUT response.

6.7. Effects of prestress on the response of the IPUT

Since the prestress has a significant influence on the resonance frequency of the IPUT [17], we expect a similar influence on the RTF as well. Additionally, as discussed in [22], the device from Fig. 7(a) had experienced buckling due to the prestress. This could result in a change in the mode shape of the IPUT, hence significantly affecting the radial displacement of the waveguides, leading to a change in the RTF, which is beyond the scope of this paper. Now we proceed to compare the NEP with the model predictions.

6.8. NEP comparison

The NEP of the IPUT is calculated using Eqs. (35), where all parameters are already obtained. The IPUT's NEP is $0.0787\,\mathrm{mPa}/\sqrt{\mathrm{Hz}}$. For a FWHM BW (148 kHz), NEP = 0.03 Pa. The total NEP value shown in [15] is 0.4 Pa, which is more than 1 order higher than the thermal noise of the IPUT. This is because, in the selected work, the thermal noise has not been explicitly extracted experimentally and the noise floor of the system is limited by the noise of the read-out system's amplifier. Figs. 15(a) and 15(b), respectively, show the variation of NEP with frequency and Q factor. Fig. 15(a) assumes a constant Q factor of 10 (experimental value) and the NEP increases with the resonance frequency of the mechanical resonator. Similarly, Fig. 15(b) assumes a constant resonance frequency of 0.76 MHz (also experimental value), and here the NEP decreases with the increase in Q factor. Nevertheless, in both cases, the experimentally obtained NEP is much higher than the thermal noise for the entire operational frequency and Q factor ranges. Thus, to further improve the performance of the IPUT, a low-noise read-out system is needed.

7. Conclusions

In this work, novel semi-analytical models were proposed to characterize the receive transfer function (RTF) and noise equivalent pressure (NEP) of integrated photonic ultrasound transducers (IPUTs) operating underwater. The models were validated by comparing them with the literature. We draw the following conclusions.

- To accurately characterize the RTF of an IPUT, it is necessary to incorporate its dynamic behavior into the acoustic model;
- To design IPUTs for the best performance, it is necessary to characterize their noise behavior along with RTF since the ratio between these parameters (signal-to-noise ratio) determines the IPUT's NEP. For applications such as medical imaging where the devices are limited by the signal-to-noise-ratio (the transmitted pulse's amplitude has an upper limit due to safety reasons), a low NEP is preferable for their better performance;
- To accurately characterize the thermal noise of the IPUT, a precise description of the RTF (Eq. (18)) is also needed as the thermal noise interacts with the outside world (detector) via the IPUT's RTF;
- Among the different factors contributing to the RTF, the waveguide's elongation and photoelastic effect have major influences;

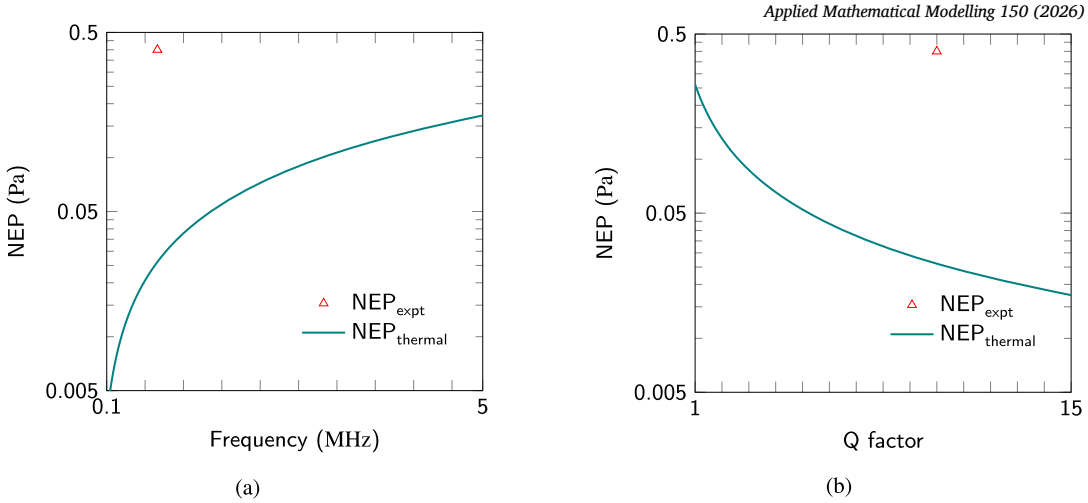

Fig. 15. Plots of NEP_{th} as a function of (a) frequency and (b) Q factor for the operational ranges of medical ultrasound applications. The red triangles in both plots indicate the experimentally obtained NEP from [15]. It can be seen that the IPUT is still limited by the noise from the photodetector for the medical ultrasound applications (frequency range from 100 kHz to 5 MHz and Q factor from 1 to 15).

- In the present case, the two predominant effects that influence the IPUT's RTF namely, the optical waveguide's physical elongation and the photoelastic effect act in the same direction due to the state of the stress tensor. In the case of a uniaxial loading of the optical waveguide, the aforementioned effects act in opposite directions as reported in the literature [50];
- The thermal noise from the fluid medium can be neglected compared to the same from the IPUT sensor since the magnitude of the former is much lower than the latter;

The model presented in this study can be extended to include complex geometric/material properties to extend the IPUT's design space further. Additionally, we can determine various parameters using this model, which can be tuned to optimize the IPUT's performance. A future direction is to use this model to design a novel IPUT device with high RTF and low NEP and validate its performance experimentally. Another interesting direction is to investigate the influence of prestress on the resonance frequency, Q-factor, RTF, and NEP of the IPUT.

CRediT authorship contribution statement

Sabiju Valiya Valappil: Writing – original draft, Validation, Software, Methodology, Investigation, Formal analysis, Conceptualization. **Peter Harmsma:** Writing – review & editing, Validation, Supervision, Resources, Methodology, Investigation, Funding acquisition. **Maurits van der Heiden:** Writing – review & editing, Supervision, Funding acquisition. **Martin Verweij:** Writing – review & editing, Supervision, Funding acquisition. **Paul van Neer:** Writing – review & editing, Visualization, Supervision, Methodology, Funding acquisition.

Declaration of competing interest

The authors declare the following financial interests/personal relationships which may be considered as potential competing interests: Martin Verweij reports financial support was provided by Dutch Research Council with the grant number NWA-1160.18.095. If there are other authors, they declare that they have no known competing financial interests or personal relationships that could have appeared to influence the work reported in this paper.

Acknowledgement

The authors greatly appreciate the support from the funding partner Nederlandse Organisatie voor Wetenschappelijk Onderzoek (NWO) for the grant entitled "Opto acoustic sensor and ultrasonic microbubbles for dosimetry in proton therapy" with the grant number NWA-1160.18.095.

Data availability

The raw data supporting this study's findings are available from the corresponding author on request.

References

[1] Aladin Carovac, Fahrudin Smajlovic, Dzelaludin Junuzovic, Application of ultrasound in medicine, Acta Inform. Med. 19 (3) (September 2011) 168–171.

[2] Bruce W. Drinkwater, Paul D. Wilcox, Ultrasonic arrays for non-destructive evaluation: a review, NDT E Int. 39 (7) (2006) 525–541.
[3] M.L. Sanderson, H. Yeung, Guidelines for the use of ultrasonic non-invasive metering techniques, Flow Meas. Instrum. 13 (4) (2002) 125–142.
[4] Alessio Carullo, Marco Parvis, An ultrasonic sensor for distance measurement in automotive applications, IEEE Sens. J. 1 (2001) 143.
[5] T.S. Awad, H.A. Moharram, O.E. Shaltout, D. Asker, M.M. Youssef, Applications of ultrasound in analysis, processing and quality control of food: a review, Food Res. Int. 48 (2) (2012) 410–427.
[6] Global Market Insight, Diagnostic ultrasound market share: Statistics report, 2023-2032, 2022.
[7] Markets and Markets, Ultrasound market by technology, global forcast to 2028, 2023.
[8] James F. Tressler, Sedat Alkoy, Robert E. Newnham, Piezoelectric sensors and sensor materials, J. Electroceram. 2 (4) (Dec. 1998) 257–272.
[9] Afshin Kashani Ilkhechi, Christopher Ceroici, Zhenhao Li, Roger Zemp, Transparent capacitive micromachined ultrasonic transducer (cmut) arrays for real-time photoacoustic applications, Opt. Express 28 (9) (Apr. 2020) 13750–13760.
[10] Joontaek Jung, Wonjun Lee, Woojin Kang, Eunjung Shin, Jungho Ryu, Hongsoo Choi, Review of piezoelectric micromachined ultrasonic transducers and their applications, J. Micromech. Microeng. 27 (11) (Sep. 2017) 113001.
[11] Wenfeng Xia, Daniele Piras, Johan C.G. van Hespen, Spiridon van Veldhoven, Christian Prins, Ton G. van Leeuwen, Wiendelt Steenbergen, Srirang Manohar, An optimized ultrasound detector for photoacoustic breast tomography, Med. Phys. 40 (3) (2013) 032901.
[12] Rayyan Manwar, Karl Kratkiewicz, Kamran Avanaki, Overview of ultrasound detection technologies for photoacoustic imaging, Micromachines 11 (7) (July 2020) 692.
[13] Wouter J. Westerveld, Md. Mahmud-Ul-Hasan, Rami Shnaiderman, Vasilis Ntziachristos, Xavier Rottenberg, Simone Severi, Veronique Rochus, Sensitive, small, broadband and scalable optomechanical ultrasound sensor in silicon photonics, Nat. Photonics 15 (5) (May 2021) 341–345.
[14] Boling Ouyang, Yanlu Li, Marten Kruidhof, Roland Horsten, Koen W.A. van Dongen, Jacob Caro, On-chip silicon Mach–Zehnder interferometer sensor for ultrasound detection, Opt. Lett. 44 (8) (Apr. 2019) 1928–1931.
[15] S.M. Leinders, W.J. Westerveld, J. Pozo, P.L.M.J. van Neer, B. Snyder, P. O'Brien, H.P. Urbach, N. de Jong, M.D. Verweij, A sensitive optical micro-machined ultrasound sensor (omus) based on a silicon photonic ring resonator on an acoustical membrane, Sci. Rep. 5 (1) (Sep. 2015) 14328.
[16] Roelof Jansen, Veronique Rochus, Jeroen Goyvaerts, Guy A.E. Vandenbosch, Bob Voort, Pieter Neutens, John M. O'Callaghan, Harrie A.C. Tilmans, Xavier Rottenberg, Micro-opto-mechanical pressure sensor (momps) in sin integrated photonics platform, 2016.
[17] V. Rochus, R. Jansen, R. Haouari, B. Figeys, V. Mukund, F. Verhaegen, J. Goyvaerts, P. Neutens, J. O' Callaghan, A. Stassen, S. Lenci, X. Rottenberg, Modelling and design of micro-opto-mechanical pressure sensors in the presence of residual stresses, in: 2017 18th International Conference on Thermal, Mechanical and Multi-Physics Simulation and Experiments in Microelectronics and Microsystems (EuroSimE), 2017, pp. 1–5.
[18] Maja Zunic, Wouter J. Westerveld, Pieter Gijsenbergh, Yongbin Jeong, Alessio Miranda, John O'Callaghan, Hamideh Jafarpoorchekab, Emmanuel Vander Poorten, Xavier Rottenberg, Roelof Jansen, Veronique Rochus, Design of a micro-opto-mechanical ultrasound sensor for photoacoustic imaging, in: 2020 21st International Conference on Thermal, Mechanical and Multi-Physics Simulation and Experiments in Microelectronics and Microsystems (EuroSimE), 2020, pp. 1–8.
[19] V. Rochus, R. Jansen, J. Goyvaerts, P. Neutens, J. O'Callaghan, X. Rottenberg, Fast analytical model of mzi micro-opto-mechanical pressure sensor, J. Micromech. Microeng. 28 (6) (Mar. 2018) 064003.
[20] V. Rochus, W.J. Westerveld, B. Figeys, X. Rottenberg, R. Jansen, Simulation and design of an optical accelerometer, in: 2019 20th International Conference on Thermal, Mechanical and Multi-Physics Simulation and Experiments in Microelectronics and Microsystems (EuroSimE), 2019, pp. 1–6.
[21] H. Gao, C.H. Huang, W. Westerveld, R. Haouari, B. Troia, F. Verhaegen, R. Jansen, B. Figeys, X. Rottenberg, V. Rochus, Simulation and characterization of a high-sensitive micro-opto-mechanical microphone, in: 2018 19th International Conference on Thermal, Mechanical and Multi-Physics Simulation and Experiments in Microelectronics and Microsystems (EuroSimE), 2018, pp. 1–4.
[22] W.J. Westerveld, S.M. Leinders, P.L.M.J. van Neer, H.P. Urbach, N. de Jong, M.D. Verweij, X. Rottenberg, V. Rochus, Optical micro-machined ultrasound sensors with a silicon photonic resonator in a buckled acoustical membrane, in: 2019 20th International Conference on Thermal, Mechanical and Multi-Physics Simulation and Experiments in Microelectronics and Microsystems (EuroSimE), 2019, pp. 1–7.
[23] Senlin Zhang, Jian Chen, Sailing He, Novel ultrasound detector based on small slot micro-ring resonator with ultrahigh q factor, Opt. Commun. 382 (2017) 113–118.
[24] Youngseop Lee, Hao F. Zhang, Cheng Sun, Highly sensitive ultrasound detection using nanofabricated polymer micro-ring resonators, Nano Converg. 10 (1) (Jun. 2023) 30.
[25] T.W. Allen, J. Silverstone, N. Ponnampalam, T. Olsen, A. Meldrum, R.G. DeCorby, High-finesse cavities fabricated by buckling self-assembly of a-si/sio2 multi-layers, Opt. Express 19 (20) (Sep. 2011) 18903–18909.
[26] M.H. Bitarafan, H. Ramp, T.W. Allen, C. Potts, X. Rojas, A.J.R. MacDonald, J.P. Davis, R.G. DeCorby, Thermomechanical characterization of on-chip buckled dome Fabry–Perot microcavities, J. Opt. Soc. Am. B 32 (6) (Jun. 2015) 1214–1220.
[27] Peter R. Saulson, Thermal noise in mechanical experiments, Phys. Rev. D 42 (Oct. 1990) 2437–2445.
[28] Charles H. Henry, Rudolf F. Kazarinov, Quantum noise in photonics, Rev. Mod. Phys. 68 (Jul. 1996) 801–853.
[29] T.J. Kippenberg, K.J. Vahala, Cavity optomechanics: back-action at the mesoscale, Science 321 (5893) (2008) 1172–1176.
[30] Malcolm B. Gray, Daniel A. Shaddock, Charles C. Harb, Hans-A. Bachor, Photodetector designs for low-noise, broadband, and high-power applications, Rev. Sci. Instrum. 69 (11) (1998) 3755–3762.
[31] U. Keller, C.E. Soccolich, G. Sucha, M.N. Islam, M. Wegener, Noise characterization of femtosecond color-center lasers, Opt. Lett. 15 (17) (Sep. 1990) 974–976.
[32] Joindot Irène, Measurements of relative intensity noise (rin) in semiconductor lasers, J. Phys. III 2 (9) (1992) 1591–1603.
[33] Davuluri Sankar, Quantum optomechanics without the radiation pressure force noise, Opt. Lett. 46 (4) (Feb. 2021) 904–907.
[34] Lingze Duan, Thermal noise-limited fiber-optic sensing at infrasonic frequencies, IEEE J. Quantum Electron. 51 (2) (2015) 1–6.
[35] G.J. Hornig, K.G. Scheuer, E.B. Dew, R. Zemp, R.G. DeCorby, Ultrasound sensing at thermomechanical limits with optomechanical buckled-dome microcavities, Opt. Express 30 (18) (Aug. 2022) 33083–33096.
[36] Hao Yang, Xuening Cao, Zhi-Gang Hu, Yimeng Gao, Yuechen Lei, Min Wang, Zhanchun Zuo, Xiulai Xu, Bei-Bei Li, Micropascal-sensitivity ultrasound sensors based on optical microcavities, arXiv preprint, arXiv:2211.07965, 2022.
[37] Alexander G. Krause, Martin Winger, Tim D. Blasius, Qiang Lin, Oskar Painter, A high-resolution microchip optomechanical accelerometer, Nat. Photonics 6 (11) (Nov. 2012) 768–772.
[38] Jonathan Y. Lee, Qiang Lin, Noise analysis in optomechanical inertial sensors, in: 2016 IEEE International Symposium on Inertial Sensors and Systems, 2016, pp. 132–135.
[39] Georg Wissmeyer, Miguel A. Pleitez, Amir Rosenthal, Vasilis Ntziachristos, Looking at sound: optoacoustics with all-optical ultrasound detection, Light: Sci. Appl. 7 (1) (Aug. 2018) 53.
[40] M. Huang, Stress effects on the performance of optical waveguides, Int. J. Solids Struct. 40 (7) (2003) 1615–1632.
[41] Allan D. Pierce, Acoustics: an Introduction to Its Physical Principles and Applications, Springer, 2019.
[42] Anthony Bedford, Douglas S. Drumheller, Introduction to Elastic Wave Propagation, Springer Nature, 2023.
[43] Gang Bao, Yixian Gao, Peijun Li, Time-domain analysis of an acoustic–elastic interaction problem, Arch. Ration. Mech. Anal. 229 (2) (Aug. 2018) 835–884.
[44] Graham T. Reed, Andrew P. Knights, Silicon Photonics: an Introduction, John Wiley & Sons, 2004.
[45] Tamma Satya Narasimhamurty, Photoelastic and Electro-Optic Properties of Crystals, Springer Science & Business Media, 2012.
[46] Paul G. Huray, Maxwell's Equations, John Wiley & Sons, 2009.

[47] Xavier Gonze, Douglas C. Allan, Michael P. Teter, Dielectric tensor, effective charges, and phonons in α-quartz by variational density-functional perturbation theory, Phys. Rev. Lett. 68 (Jun. 1992) 3603–3606.
[48] L.S. Hounsome, R. Jones, M.J. Shaw, P.R. Briddon, Photoelastic constants in diamond and silicon, Phys. Status Solidi (a) 203 (12) (2006) 3088–3093.
[49] Jeiping Xu, Robert Stroud, Acousto-optic devices: principles, design, and applications, 1992.
[50] Wouter J. Westerveld, Suzanne M. Leinders, Pim M. Muilwijk, Jose Pozo, Teun C. van den Dool, Martin D. Verweij, Mirvais Yousefi, H. Paul Urbach, Characterization of integrated optical strain sensors based on silicon waveguides, IEEE J. Sel. Top. Quantum Electron. 20 (4) (2014) 101–110.
[51] David Keith Chalmers MacDonald, Noise and Fluctuations: an Introduction, Courier Corporation, 2006.
[52] H.J. Butt, M. Jaschke, Calculation of thermal noise in atomic force microscopy, Nanotechnology 6 (1) (Jan. 1995) 1.
[53] Horace Lamb, On the vibrations of an elastic plate in contact with water, Proc. R. Soc. Lond. Ser. A, Contain. Pap. Math. Phys. Character 98 (690) (1920) 205–216.
[54] M. Amabili, M.K. Kwak, Free vibrations of circular plates coupled with liquids: revising the lamb problem, J. Fluids Struct. 10 (7) (1996) 743–761.
[55] Yves Pomeau, Jarosław Piasecki, The Langevin equation, C. R. Phys. 18 (9) (2017) 570–582, Science in the making: the Comptes rendus de l'Académie des sciences throughout history.
[56] B.D. Hauer, C. Doolin, K.S.D. Beach, J.P. Davis, A general procedure for thermomechanical calibration of nano/micro-mechanical resonators, Ann. Phys. 339 (2013) 181–207.
[57] Michael Peter Norton, Denis G. Karczub, Fundamentals of Noise and Vibration Analysis for Engineers, Cambridge University Press, 2003.
[58] William H. Press, Saul A. Teukolsky, William T. Vetterling, Brian P. Flannery, Numerical recipes, in: The Art of Scientific Computing, 3rd edition, Cambridge University Press, 2007.
[59] T.R. Albrecht, P. Grütter, D. Horne, D. Rugar, Frequency modulation detection using high-q cantilevers for enhanced force microscope sensitivity, J. Appl. Phys. 69 (2) (1991) 668–673.
[60] Wouter J. Westerveld, Silicon photonic micro-ring resonators to sense strain and ultrasound, Ph.D., Delft University of Technology, 2014.
[61] J. Chung, G.M. Hulbert, A time integration algorithm for structural dynamics with improved numerical dissipation: the generalized-α method, J. Appl. Mech. 60 (2) (06 1993) 371–375.
[62] Mode solvers – waveguide CAD software – FIMMWAVE – photond.com, https://www.photond.com/products/fimmwave.htm. (Accessed 10 March 2024).